Dynamic superresolution by Bayesian nonparametric image processing

Ioannis Sgouralis[1], Ameya P. Jalihal[2], Lance W.Q. Xu (徐伟青)[3,4], Nils G. Walter[2], and Steve Pressé[3,4,5,*]

[1]Department of Mathematics, University of Tennessee, Knoxville, TN 37996, USA
[2]Single Molecule Analysis Group and Center for RNA Biomedicine, Department of Chemistry, University of Michigan, Ann Arbor, MI 48109, USA
[3]Center for Biological Physics, Arizona State University, Tempe, AZ 85287, USA
[4]Department of Physics, Arizona State University, Tempe, AZ 85287, USA
[5]School of Molecular Sciences, Arizona State University, Tempe, AZ 85287, USA
[*]Corresponding author (email: spresse@asu.edu)

Abstract

Assessing dynamic processes at single molecule scales is key toward capturing life at the level of its molecular actors. Widefield superresolution methods, such as STORM, PALM, and PAINT, provide nanoscale localization accuracy, even when distances between fluorescently labeled single molecules ("emitters") fall below light's diffraction limit. However, as these superresolution methods rely on rare photophysical events to distinguish emitters from both each other and background, these methods are largely limited to static samples. In contrast, here we leverage spatiotemporal correlations of dynamic widefield imaging data to extend superresolution to simultaneous multiple emitter tracking without relying on photodynamics even as emitter distances fall from one another below their diffraction limit. That is, we simultaneously determine emitter numbers and their tracks (localization and linking) with the same localization resolution per frame as static emitters using widefield superresolution microscopy (≈50 nm). We demonstrate our results for both *in vivo* data and, for benchmarking purposes, on synthetic data as well. To achieve this, we avoid the existing tracking paradigm relying on completely or partially separating the tasks of emitter number determination, localization of emitters and linking emitter positions across frames. Instead, we employ Bayesian nonparametrics and develop a fully joint posterior distribution over the quantities of interest, including emitter tracks and their total, otherwise unknown, number. Our posterior allows us to estimate emitter numbers alongside their associated tracks, with uncertainty propagated from multiple origins including shot and detector noise, pixelation, and out-of-focus motion.

Keywords: Fluorescence microscopy, Superresolution microscopy, Nanoscopy, Single molecule tracking, Image analysis, Bayesian nonparametrics

Introduction

Characterizing macromolecular assembly kinetics [6], quantifying intracellular biomolecular motility [40, 21, 22], or interrogating pairwise biomolecular interactions [46] requires accurate decoding of spatiotemporal processes approaching the single molecule level, *i.e.*, nm spatial and rapid, often ms, temporal scales. These tasks ideally require superresolving positions of dynamic targets, typically fluorescently labeled molecules (light emitters), to tens of nanometer spatial resolution [32, 51, 2] and, when more than one target is involved, discriminating between signals from multiple targets simultaneously.

Yet assessments by means of fluorescence experiments at the required scales suffer from inherent limitations. Such limitations often arise from the diffraction limit of light, $\approx$250 nm in the visible range, below which conventional fluorescence techniques cannot discern sufficient contrast between neighboring emitters of interest. To go beyond the limitations of conventional tools and achieve superresolution, contrast is created through structured illumination [14], structured detection [24, 55, 54, 38], the photoresponse of fluorophore labels to excitation light [32, 51, 2, 44], or combinations thereof [17, 30, 56, 1].

Here we focus on widefield *superresolution microscopy* (SRM), typically relying on fluorophore photodynamics to achieve superresolution. SRM is regularly used both *in vitro* [45, 25] and *in vivo* [51, 2, 19, 50, 29, 37]. Specific widefield SRM image acquisition protocols, such as STORM [44], PALM [2], and PAINT [45], through their associated image analyses, decode positions of light emitters separated by distances below the diffraction limit, often down to the resolution of tens of nanometers [44, 2]. These widefield SRM protocols can be broken down into three conceptual steps: (i) specimen preparation; (ii) imaging; and (iii) computational processing of the acquired images. The success of Step (iii) is ensured by both Steps (i)-(ii). In particular, in Step (i) engineered fluorophores are selected that enable the desired photodynamics; *e.g.*, photoswitching in STORM [44], photoactivation/bleaching in PALM [2], or fluorophore binding/unbinding in PAINT [45]. Step (ii) is then performed over extended periods, while awaiting rare photophysical (or binding-unbinding) events to manifest and for sufficient photons to be collected to achieve superresolved localizations in Step (iii). For well isolated bright spots, Step (iii) achieves superresolved localization [27, 32, 51] while accounting for effects such as light diffraction, resulting in spot sizes of roughly twice $0.61\lambda/\text{NA}$ (the Rayleigh diffraction limit), set by the emitter wavelength (λ) and the numerical aperture (NA) of the microscope's objective [42], as well as detector and photon shot noise, and spot pixelization.

Here we show that computation can be used to mitigate reliance on the photophysics of Step (i) and the long periods of acquisition of Step (ii) that not only limit widefield SRM largely to static samples, but may also induce sample photodamage. In fact, while a moving emitter's distribution, or smearing, of its photon budget over multiple frames and pixels may be regarded as a disadvantage in the implementation of Step (iii) above, we demonstrate conversely that such a distribution of the photon budget in both space and time provides information that can be leveraged to superresolve emitter tracks, determine emitter numbers, and help discriminate targets from their neighbors, even in the absence of photophysical events altogether; see fig. 1.

The overall input to our framework, Bayesian nonparametrics (BNP)-Track, includes both raw image sequences and information on the imaging system, and captures microscope optics and camera electronics further detailed in METHODS. In our formulation, we provide a means of estimating *unknowns* including *number of emitters and their associated tracks* and overcome this challenge specifically with Bayesian nonparametrics.

More specifically, we demonstrate BNP-Track on experimental data, detailing how the simultaneous determination of emitter numbers and tracks can be computationally achieved. We briefly compare BNP-Track's performance to diffraction-limited tracking tools here. We devote a much more detailed comparison between BNP-Track and modified competing tracking methods, including robustness analysis of both BNP-Track and competing tools, to a companion manuscript. We do so as we must impart some advantages for sake of comparison to competing tools (such as by providing competing methods with the correct number of emitters as input).

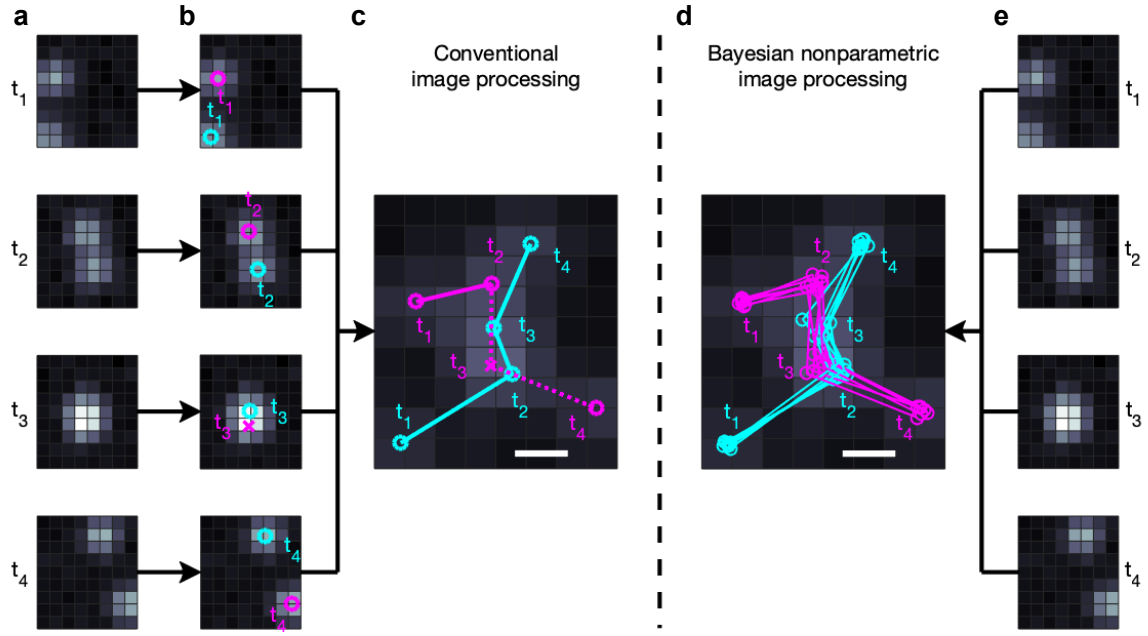

Figure 1: *A conceptual comparison between two tracking frameworks.* **a** *and* **e**, *Four frames from a timelapse dataset imaging two emitters.* **b**, *Existing tracking approaches [47, 23, 58, 34, 4, 57, 7, 13, 33, 59, 20, 3] either completely or partially separate the task of first identifying and then localizing light emitters in the field of view of each frame independently.* **c**, *Conventional approaches then link emitter positions across frames.* **d**, *Our nonparametric approach (BNP-Track) simultaneously determines the number of emitters, localizes them and links their positions across frames. In* **b-d**, *circles denote correctly identified emitters, and crosses denote missed emitters. In* **c** *and* **d**, *scale bars indicate a distance equal to the nominal diffraction limit given by the Rayleigh diffraction limit* $0.61\lambda/NA$.

Results

We begin by outlining the flow of the Results section that we break down into three subsections. We start with an analysis, using BNP-Track, of mRNA diffusing in U2OS live cells with a dual camera imaging setup (figs. 2 and 3) under single plane HILO illumination [48]. While we use the dual camera setup to verify the consistency of BNP-Track's emitter number and trajectory determination across both detectors, ground truth trajectories are fundamentally unknown. For this reason, and as is typical in tracking assessments [47, 5], we then illustrate BNP-Track on synthetic data, figs. 4 and 5, where ground truth trajectories and emitter numbers are known. Here the synthetic data being generated from ground truth trajectories we extract from the earlier analysis to which we add realistic noise (such as detector noise, shot noise, pixelization) according to the protocol detailed in Methods following the recipe from [5] and whose numerical values are directly motivated from experiments in figs. 2 and 3. Of particular interest is our ability to learn emitter numbers and track them as we systematically bring ground truth emitter tracks closer together than light's diffraction limit (fig. 5). Having established our ability to track emitters closer than light's diffraction limit, we then move to the challenging case of tracking in crowded environments (fig. 6), and show comparison to a conventional tracking method, TrackMate [47], a widely used single particle tracking tool which combines and is built upon contest leading tracking methods [5]. We find that TrackMate not only fails to surpass the diffraction limit, but it also does not learn emitter numbers. Yet learning emitter numbers is especially critical in correctly linking emitter locations across frames, especially in crowded environments. As competing tools do not learn emitter numbers, direct head-to-head comparison to other tracking tools is not possible and a detailed comparison of BNP-Track to augmented competing tools is relegated to a companion manuscript alongside detailed robustness analysis of BNP-Track.

Prior to showing results of BNP-Track, an important note on Bayesian inference is warranted. Developed within the Bayesian paradigm [49, 12, 52], BNP-Track not only provides point estimates over unknown quantities of interest, such as numbers of emitters and their associated trajectories, but also fully quantifies the uncertainty, *i.e.*, the full posterior distribution, over them. As we cannot easily visualize the output of multidimensional posteriors, by convenience, we often consider the number of emitters that maximize the posterior (though we compute probabilities of other numbers of emitters). These are termed *maximum a posteriori* (MAP) point estimates in the number of emitters. For example, emitter trajectories from the MAP number of emitters are collected and reorganized based on their similarity, as explained in appendix J.2. These selected trajectories are plotted in figs. 2 to 4. The average trajectory of each group constitutes the trajectory point estimates. As for uncertainties, we report them in terms of each quantity's credible interval.

BNP-Track superresolves sparse single-emitter tracks in vivo

Following the outline above, we illustrate how BNP-Track assesses mRNA motility *in vivo* [39] in figs. 2 and 3. As is the case for all single particle tracking applications, no ground truth trajectories are available from experimental data. For this reason, as a control as we have highlighted above, our timelapse images are collected, via a beamsplitter, on two separate detectors (cameras) and independently processed for subsequent comparison.

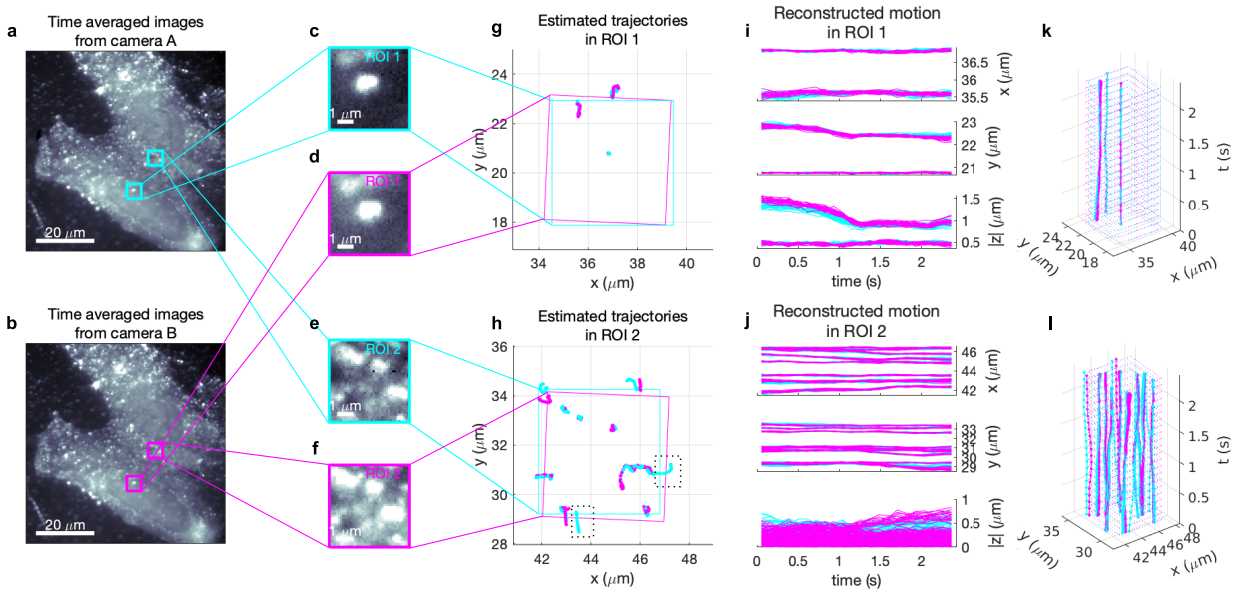

Figure 2: *BNP-Track's performances on two* $5\,\mu$m*-wide ROIs with different emitter densities from an experimental dataset of labeled mRNA diffusing in U2OS live cells using a dual camera imaging setup.* **a** *and* **b**, *The time-averages of all 22 frames analyzed from camera A and B, respectively. The selected ROIs are highlighted using squares.* **c** *and* **d**, *Zoomed-in ROI 1 from camera A and B.* **e** *and* **f**, *Zoomed-in ROI 2 from camera A and B.* **g** *and* **h**, *Estimated trajectories of the selected ROIs from both cameras with solid boxes indicating the corresponding fields of view.* **i** *and* **j**, *Reconstructed time courses for individual trajectories of the selected ROIs. The dotted boxes in* **h** *highlight two emitter trajectories only seen by camera A.* **k**, *Time course reconstruction by combining (*__i__*, top) and (*__i__*, middle).* **l**, *Time course reconstruction by combining (*__j__*, top) and (*__j__*, middle).*

In figs. 2a and 2b, we show, for illustrative purposes alone, the time averages of a sequence of 22 successive frames spanning ≈ 2.5 s of real time in both detection channels. In the data processing, we analyze the underlying frames without averaging.

We start with simple single-emitter tracking where we considered a $5\,\mu$m wide square region of interest (ROI), named as ROI 1. In ROI 1, emitters are sufficiently well separated, *i.e.*, dilute. This ROI was manually selected from the entire field of view according to the criterion that emitter point spread functions (PSFs) always be well separated in space. Figures 2c and 2d zoom in on ROI 1. The trajectory estimates are shown in fig. 2g while, in fig. 2i, all samples from the posterior are superposed. Since due to fundamental optical limitations we cannot determine whether the emitter's axial position lies above or below the focus plane, we only report the absolute value of the emitters' axial position. As evident from fig. 2g obtained using ROI 1, our method successfully identifies and localizes the same trajectories within the selected ROI in both datasets, *both cameras*. The two square ROI 1's coinciding with images from each detector appear rotated with respect to one another after image registration in post-processing. Figure 2i, again obtained using ROI 1, shows trajectories of all well separated emitters identified within this field of view. We note that the emitter near the top of ROI 1 in fig. 2g is almost always outside both the fields of view of both cameras. Although BNP-Track still reports qualitatively consistent trajectories from both cameras, we exclude this emitter in fig. 2i and further analysis.

The agreement between tracks across both cameras is quantified according to the pairing distance; further details in appendix J.2. This reveals a localization error of 73 nm in the lateral direction. Consequently, BNP-Track's average error from the ground truth (one half of the localization error) is about ≈ 37 nm, consistent with superresolution values [32, 51, 2].

As BNP-Track provides estimates of the lateral as well as the magnitude of the axial emitter position (see details in $\textsc{Methods}$), we can also assess the full localization error in 3D. This results in a 3D pairing distance of 97 nm and thus a ≈ 48 nm localization error from ground truth.

Having shown that we can track emitters in a dilute regime similar to ROI 1 of figs. 2c and 2d, we move onto the analysis of a more challenging ROI, ROI 2, (figs. 2e and 2f) where emitter PSFs now occasionally overlap. This allows us to repeat the analysis of ROI 1 albeit now for simultaneous multi-emitter tracking as we move toward a more crowded environment.

As before, for illustrative purposes alone, in figs. 2a and 2b we show time averages of a sequence of 22 successive frames spanning ≈ 2.5 s of real time. Figures 2e, 2f and 2h reflect the same information earlier described for ROI 1. As shown in Figure 2h, again, BNP-Track can track emitters even when they diffuse away from a camera's field of view. Similarly, as before, we used the pairing distance to quantify the localization error in the lateral direction. For ROI 2, the localization error is 128 nm with an error from the ground truth of about 64 nm, which remains under the nominal diffraction limit of 231 nm of our imaging apparatus. Also, as before, the localization error in 3D is now 159 nm, resulting in the error from ground truth of about 80 nm.

While we have focused on showing trajectory estimates, the method proposed here also estimates other dynamical quantities including the background photon fluxes (photon per unit area per unit time), the emitter brightness (photon per unit time), the diffusion coefficient, and the number of emitters. Estimates for these quantities are summarized in fig. 3. It is worth noting that figs. 3b and 3c show that both the system's background flux and emitter brightness vary over time, making ROI 2 more challenging. Despite our trajectories' agreement below light's diffraction limit from both cameras, discrepancies in some quantities (such as diffusion coefficient) highlight the extreme sensitivity of these quantities to small trajectory variations even below the superresolution limit. As a further example, small discrepancies in the emitter brightness estimates (fig. 3c) that we recover may be induced by dissimilarities in the optical path leading to each camera, such as uneven light splitting in our beamsplitter. Even small discrepancies in image registration can account for the differences in the estimated numbers of emitters and their diffusion coefficients as the pixels in the two datasets do not image precisely the same volumes of the specimen.

Finally, the number of emitters detected in both cameras appear to be different (fig. 3e), and the additional trajectories detected by camera A are highlighted by dotted boxes in fig. 2h. This is unsurprising for three

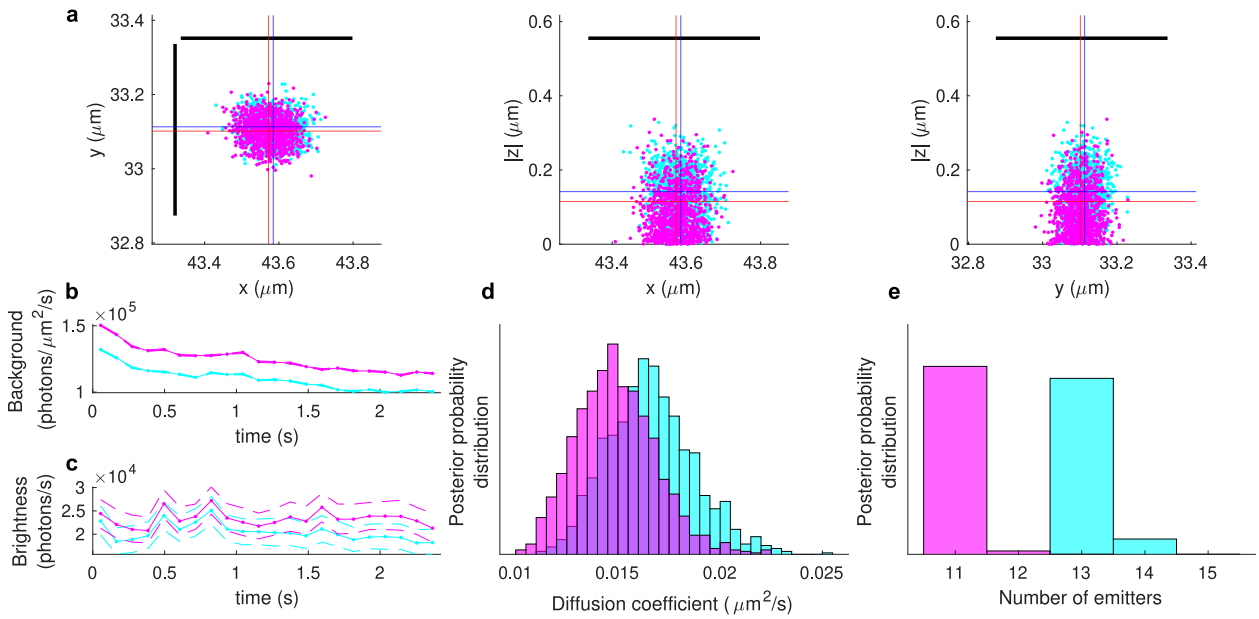

Figure 3: *More of BNP-Track's outputs for ROI 2 of figs. 2e and 2f. The color scheme here follows the same convention as in fig. 2 (cyan for camera A and magenta for camera B).* **a**, *Localization estimates in the lateral and axial directions at a selected frame of a selected emitter. Dots indicate individual positions sampled from the joint posterior distribution (as detailed in* METHODS*) and blue and red crosses indicate average values for cyan and magenta, respectively. The black line segments mark the diffraction limit in the lateral direction.* **b** *and* **c**, *Estimated background photon fluxes and emitter brightnesses for both cameras throughout the course of imaging. Dotted lines represent median estimates and dashed lines map the 1%-99% credible interval.* **d** *and* **e**, *The posterior distributions of diffusion coefficient and number of emitters for both cameras.*

reasons. Firstly, as discussed in the previous paragraph, the two cameras have different fields of view, and it is therefore reasonable to observe a discrepancy in the number of detected emitters. Secondly, as highlighted by the dotted boxes in fig. 2h, a significant portion of the two extra trajectories lie outside the fields of view of both cameras. Furthermore, as background noise can be mathematically modeled by out-of-focus emitters, and since two cameras draw slightly different conclusions on background photon emission rates and molecular brightnesses (figs. 3b and 3c), this may also naturally lead to slightly different estimates of the number of emitters especially out-of-focus. Put differently, BNP-Track not only learns about positions of in-focus emitters but uses what it learns on in-focus emitters to extrapolate outside the field of view or the focal plane. However, in such regions the number of photons used by BNP-Track to draw inferences on trajectories is necessarily limited.

Benchmarking BNP-Track with synthetic data

We also validate our method using synthetically generated data where ground truth trajectories are known. In order to generate realistic timelapse image data, we start from the estimated trajectories of the MAP joint sample of camera A's ROI 2 as our ground truth. We then add optical artifacts and noise according to METHODS. Parameters used in the simulations are either identical to those of experiments (NA, pixel size, frame rate) or, in the case of brightness and background photon flux, identical to those estimated from experiment (fig. 3).

The results of our analysis are shown in fig. 4. Figure 4a shows the ground truth in magenta and the estimated trajectories in cyan with a unique trajectory highlighted as a wider magenta line. To help with visualization, fig. 4b focuses on the highlighted magenta trajectory only. In fig. 4c, we further quantify the localization at $0.5\,\mathrm{s}$

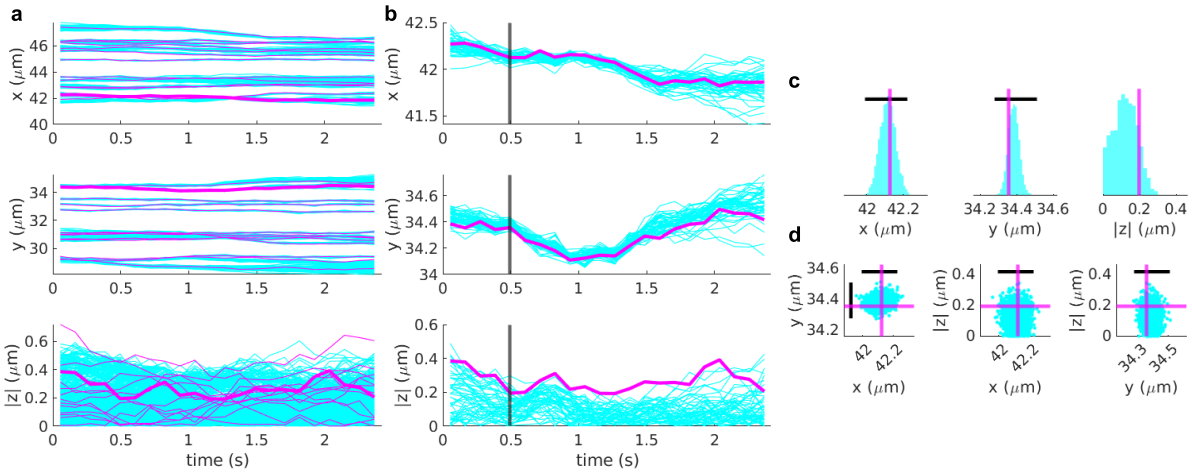

Figure 4: *BNP-Track's performance using synthetic data. Through all panels, BNP-Track's samples are in cyan and ground truths are in magenta.* **a**, *BNP-Track's reconstructions of time courses for all emitters' trajectories.* **b**, *The trajectory reconstructions of an out-of-focus emitter. This emitter's ground truth trajectory is highlighted in* **a** *with thicker lines.* **c**, *Posterior distributions of individual localizations corresponding to the time level highlighted in* **b** *with black vertical lines. The black line segments mark the lateral diffraction limit in* **c**. **d**, *Sampled emitter locations in the lateral and axial directions. Again, crosses show estimate means and black line segments mark the lateral diffraction limit.*

(indicated by a black vertical line in fig. 4b). The histograms appearing in fig. 4c show the lateral and axial localization error determined from the pairing distance with ground truth, and the lateral localization error is compared to the nominal diffraction limit. The scatter plots in fig. 4d quantify co-localization in all three spatial directions.

Next, in fig. 5, we explore how closely two emitters can move in space to each other while retaining BNP-Track's ability to discriminate between them. To test this, a pair of estimated trajectories from ROI 2 of fig. 2 were used as ground truth for the simulation of synthetic data (shown in figs. 5a to 5f) using the same parameters as in fig. 4. From figs. 5a to 5f, the mean displacement between emitters is gradually decreased. Figures 5g to 5l show reconstructed trajectories and comparison with the ground truth. Remarkably, the localization error estimated from the total pairing distance remains ≈ 40 nm in 2D and ≈ 50 nm in 3D throughout the simulated scenarios and increases, albeit only slightly, below the diffraction limit. Figures 5m to 5r show characteristic estimates on the same datasets shown in figs. 5a to 5f obtained from TrackMate. TrackMate results are also compared with the ground truth using localization errors. In using TrackMate, we note that: (i) TrackMate is manually tuned (for instance, the number of emitters is adjusted to obtain the best matching trajectories); and (ii) the lateral localization errors of TrackMate are calculated without taking into account missing segments or whole trajectories. Both of these factors provide TrackMate with significant advantages. Even so, BNP-Track's localization error is smaller under most circumstances. Detailed quantitative comparisons generated by the Tacking Performance Measures plugin [5] in Icy [9] are provided in tables A.1 to A.6 and more extensive comparisons are detailed in a companion manuscript.

It is expected that existing tracking methods, such as TrackMate, should fail to resolve emitters with separations close to or below the diffraction limit (as seen in figs. 5p to 5r). However, TrackMate also misses trajectory segments even when the mean lateral displacements between trajectories lie well above the diffraction limit (as seen in figs. 5m to 5o). This is because parts of the emitter trajectories move out-of-focus, which can be directly observed from the following: (i) in figs. 5a to 5c, one emitter's average intensity is lower and more wide-spread, and (ii) in figs. 5g to 5i, some $|z|$ positions are around 200 nm from the focal plane. Meanwhile, by leveraging spatiotemporal information, BNP-Track is still capable of tracking these out-of-focus emitters. In the companion

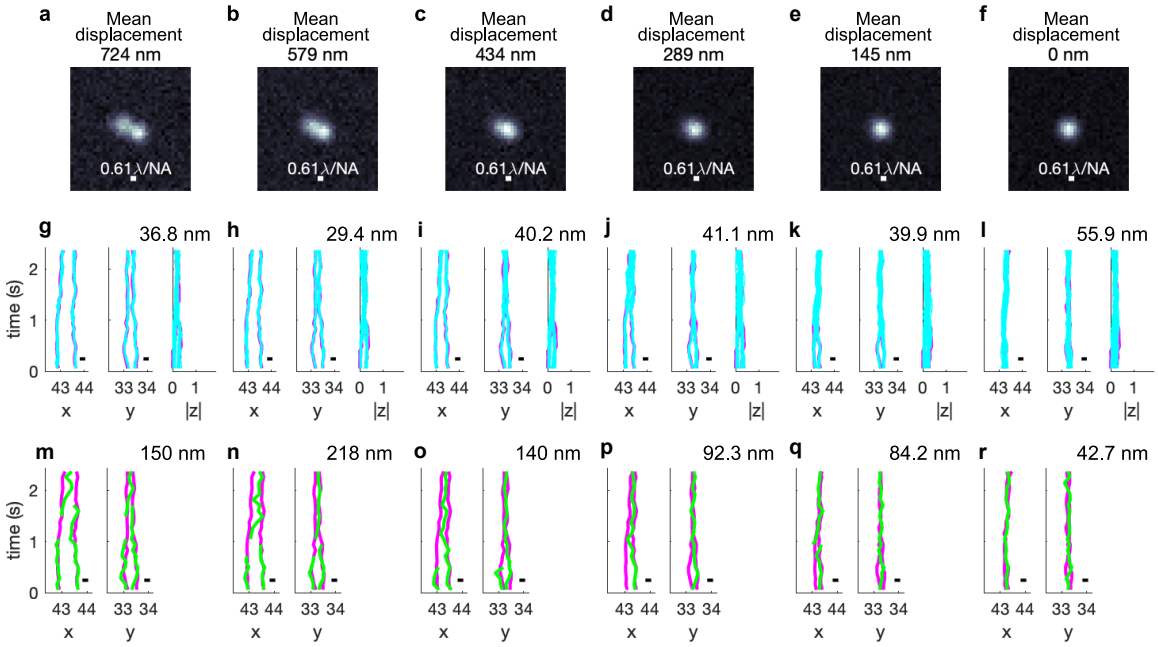

Figure 5: *Benchmarks of BNP-Track on the mean displacement between two tracks. TrackMate tracks are also provided for comparison.* **a-f**, *The time-averaged images for the simulated scenarios. The mean displacements are* $724\,\text{nm}$ *(***a***),* $579\,\text{nm}$ *(***b***),* $434\,\text{nm}$ *(***c***),* $289\,\text{nm}$ *(***d***),* $145\,\text{nm}$ *(***e***), and* $0\,\text{nm}$ *(***f***).* **g-l**, *BNP-Track's reconstructed trajectories for all coordinates. Reconstructed trajectories are in cyan and the ground truths are in magenta. Lateral localization errors are listed at the top right of each panel.* **m-r**, *TrackMate's estimated trajectories (green) of the same datasets with the ground truths (magenta). Lateral localization errors are listed at the top right of each panel, with missing segments excluded. Also, no axial results are plotted in (***m-r***) as TrackMate does not provide axial trajectories for 2D images.*

manuscript, we detail how this is achieved.

BNP-Track's performance in increasingly crowded environments

Here in fig. 6a, similar to figs. 2a and 2b, we first present time-averaged images from both detectors. These images reveal the presence of approximately tens of emitters dispersed throughout the fields of view. Additionally, this ROI contains closely positioned and out-of-focus emitters, as evidenced by the irregular shapes and lower intensities of certain bright regions, respectively.

In fig. 6b, we present the results of BNP-Track for both cameras A and B. The two cameras observe different volumes within the cell as their fields of view are offset by approximately $1.5\,\mu$m and rotated by 5°. This complex dataset provided unique challenges for BNP-Track to overcome. To provide an assessment of BNP-Track's performance that we can reliably compare to TrackMate, we selected the in-focus emitters in the overlapping region and calculated the pairing distance between tracks. We define "in-focus" emitters as emitters whose estimated z position is within $150\,\text{nm}$ of the in-focus ($z = 0$) plane. We are encouraged by the results, as the localization error derived from this pairing distance is approximately $136.4\,\text{nm}$, which corresponds to a localization error of $68.2\,\text{nm}$ compared to the ground truth. These results are consistent with the performance for ROI 2 in fig. 2.

We also used TrackMate to analyze the timelapse data depicted in figs. 6a and 6b. The analysis results for camera A are illustrated in figs. 6c and 6d. Specifically, for fig. 6c, we set a high localization quality threshold to

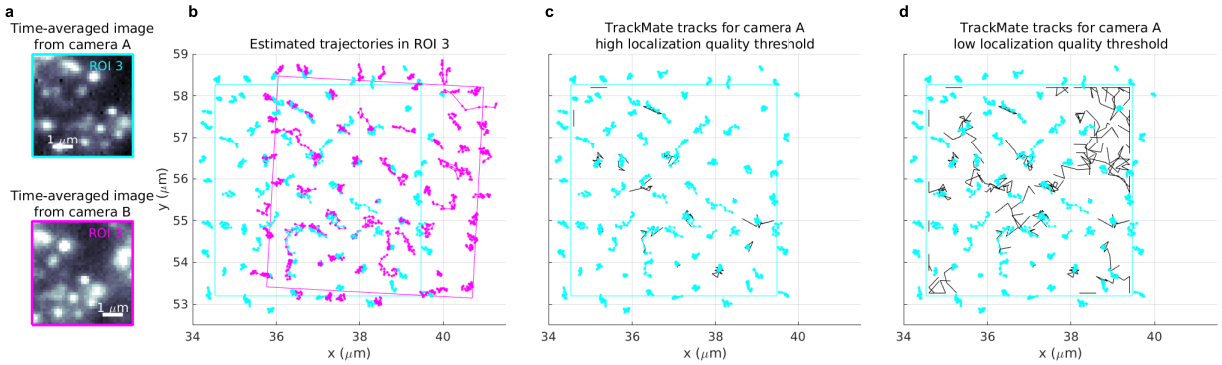

Figure 6: *BNP-Track can track in more crowded environment.* **a**, *Time-averaged images over 22 frames from both cameras show that there are many diffraction-limited emitters within the fields of view.* **b**, *BNP-Track's tracking results after registering fields of view.* **c**, *A comparison between BNP-Track's result and TrackMate's result with a high localization quality threshold for the data from camera A. TrackMate tracks are in black; see [47] for the definition of quality.* **d**, *A comparison between BNP-Track's result and TrackMate's result with a low localization quality threshold for the data from camera A. TrackMate tracks are in black. The axis ranges in (***b-d***) are the same.*

minimize spurious detections, which led to almost 10 matching tracks with BNP-Track which identified roughly 70 emitters. Nonetheless, most of the emitters were missed by TrackMate. Conversely, in fig. 6d, we lowered the quality threshold to capture more detections. However, despite tuning the linking step accordingly, TrackMate's linking errors increased significantly due to the densely crowded environment. Consistent with our findings thus far, figs. 6c and 6d once again underscores BNP-Track's efficacy in tracking in crowded environments.

Discussion

We here present an image processing framework, BNP-Track, that superresolves diffusing particles *n vivo* without the need for complex fluorophore photodynamics. Our framework analyzes timelapse image measurements from diffraction limited light emitters throughout image acquisition. BNP-Track thereby extends the scope of widefield SRM by leveraging spatiotemporal information encoded across frames and pixels. Additionally, BNP-Track unifies many existing approaches to localization microscopy and single-particle tracking and extends beyond them by decoupling image acquisition from image processing by computationally estimating emitter numbers; see fig. 5.

By operating in three interlaced stages (preparation, imaging, processing) existing approaches to widefield SRM estimate locations of individual static emitters with a generally accepted accuracy of ≈ 50 nm or less [32, 51, 2]. Such accuracy for widefield applications is a significant improvement relative to the diffraction limit of conventional microscopy, ≈ 250 nm. Although our processing framework cannot lift the limitations imposed by optics, nor eliminate the degradation induced by noise, our framework can significantly extend our ability to estimate emitter numbers and tracks from existing images with uncertainty both for easier in-focus cases and more challenging cases out-of-focus and partly out of the field of view. In particular, because our framework provides full distributions over unknowns, it readily computes error bars associated with emitter numbers warranted by images (*e.g.*, figs. 3 and 4), localization events for both isolated emitters and emitters closer than light's diffraction limit, and other parameters including diffusion coefficients.

It is well known that any tracking method will face challenges in certain circumstances, such as out-of-focus motion, crowded environments, or detector saturation. In such cases, the available information may be insufficient for tracking purposes. Although quantifying when BNP-Track fails is highly dependent on the specific circumstance, we contend that its performance can serve as a measure of whether a timelapse dataset provides enough information for emitter tracking. This is because BNP-Track incorporates spatiotemporal information by modeling the entire

process from emitter motion to photon detection, thus maximizing the amount of extracted information. If BNP-Track fails to track in a particular system, conventional tracking methods are also very likely to fail, indicating the need for an alternative experimental protocol.

The analysis of a field of view like those shown in Results ($5\,\mu$m $\times$ $5\,\mu$m or about 1500 pixels, and 22 frames) requires about 300 min of computational time on an *average laptop computer*. The computational cost of our analysis scales linearly with the product of the number of frames, total pixel number, and the total number of emitters, $O(NPB)$. Larger scale applications are within the realm of existing computational capacity; however, algorithmic improvements and computational optimization will be required to speed up execution time. Despite its higher computational cost compared to current single-particle tracking methods, we argue two points. Firstly, as demonstrated in fig. 5, cheaper conventional tracking methods often fail altogether. Secondly, our method's time of execution is primarily computational wall-time as BNP-Track is unsupervised and largely free from manual tuning. This is by contrast to methods such as TrackMate used in the generation of fig. 5 that require detailed manual tuning and thresholding for proper execution, as detailed more extensively in a companion manuscript.

While we have focused on the conceptual basis for how to beat the diffraction limit computationally, with more extensive changes to our processing framework, the methods herein can also be adapted to accommodate specialized illumination modalities including TIRF [10], HILO [48], or light-sheet [43], or even multi-color imaging. None of these adaptations break the unifying theme of Bayesian nonparametric tracking which relies on the joint assessment of three steps characteristic of traditional single-particle tracking (emitter number determination, emitter localization and linking). Along these same lines, in Methods, we made many common modeling choices and used parameters common in experiments. For example, we used an EMCCD detector model and assumed a Gaussian PSF. Other choices can be made by simply changing the mathematical form of the detector model or the PSF provided these assume known, pre-calibrated, forms. None of these changes break the conceptual features of BNP-Track. Similarly, another assumption made in this study is that BNP-Track considers only a Brownian motion model, and one may question its performance when other motion models are present. However, throughout Results, we have demonstrated that BNP-Track yields accurate tracking results consistent across two cameras for an experimental dataset with an unknown emitter motion model, despite assuming Brownian motion. This suggests that BNP-Track may remain robust under potentially other alternative motion models.

Currently, post-processing tools are frequently utilized to extract useful information from single-particle tracking datasets, such as diffusion dynamics and diffusive states. These tools range from simple approaches, such as mean square displacement, to more complex methods, such as Spot-On [15] and SMAUG [26]. Since our framework already takes into account the motion model during emitter tracking, it is inherently compatible with these post-processing tools. It is also now even conceivable that we may use our output as a training set for neural nets [31] or start making predictions of molecular trajectories in dense environments [11], such as fig. 6, previously considered outside the scope of existing tools.

Taken together, the framework we present is the first proof-of-principle demonstration that computation feasibly achieves superresolution of evolving targets by avoiding the modular approximations of the existing tracking paradigm which has thus far limited tracking to dilute and in-focus samples.

Methods

Image processing

As we demonstrate in Results, our analysis' goal is the determination of the probability distribution termed the posterior, $p(\theta|W)$. In this distribution, we use θ to gather the unknown quantities of interest, for instance emitter tracks and photon emission rates, and W to gather the data under processing, for instance timelapse images.

Below we present how this distribution is derived as well as its underlying assumptions.

To facilitate the presentation, we follow a description in *two parts*. First, we present a detailed formulation of the physical processes involved in the formation of the acquired images necessary in quantitative analysis earlier discussed. This formulation captures microscope optics and camera electronics and can be further modified to accommodate more specialized imaging setups. In the formulation, the *unknowns* of interest are encoded by parameters. Second, we present the mathematical tools needed to estimate values for such unknown parameters. That is, we address the core challenge in SRM arising from the *unknown number of emitters and their associated positions* and, to overcome this challenge specifically, we apply Bayesian nonparametrics. Our approach in the second part is different from likelihood-based approaches, currently employed in localization microscopy, and is ultimately what allows us to relax SRM's photodynamical requirements.

As several of the notions involved in our description are stochastic, for example parameters with unknown values and random emitter dynamics, we use probabilistic descriptions. Although our notation is standard to the statistics community, we provide an introduction more appropriate for a broader audience in the SUPPORTING INFORMATION.

Model description

Our starting point consists of image measurements obtained in a SRM experiment denoted by w_n^p, where subscripts $n = 1, \ldots, N$ indicate the exposures and superscripts $p = 1, \ldots, P$ indicate pixels. For example, w_2^3 denotes the *raw* image value, typically reported in ADU or counts and stored in TIFF format, measured in pixel 3 during the second exposure. Similarly, $w_2^{1:P}$ denotes every image value (*i.e.*, entire frame) measured during the second exposure. Since the image values are related to the specimen under imaging, our goal from now on is to develop a mathematical model that encodes the physical processes relating the specimen under imaging *with* the acquired measurements.

Noise The recorded images mix electronic signals that depend only stochastically on an average amount of incident photons [41, 28, 18, 16]. For commercially available cameras, the overall relationship, from incident photons to recorded images, is linear and contaminated with multiplicative noise that results from shot noise, amplification and readout. Our formulation below applies to image data acquired with cameras of the EMCCD type, as commonly used in superresolution imaging [32, 18], though the expression below can be modified to accommodate other camera types. Here, in our formulation

$$w_n^p | u_n^p \sim \text{Normal}\left(\mu + \xi u_n^p, \upsilon + f\xi^2 u_n^p\right)$$

where u_n^p is the average number of photons incident on pixel p during exposure n. The parameter f is a camera dependent excess noise factor and ξ is the overall gain that combines the effects of quantum efficiency, pre-amplification, amplification and quantization. The values of μ, υ, ξ, and f are specific to the camera that acquires the images of interest and their values can be calibrated as we describe in SUPPORTING INFORMATION.

Pixelization As shot-noise is already captured, u_n^p depends deterministically on the underlying photon flux

$$u_n^p = \int_{t_n^{\min}}^{t_n^{\max}} dt \iint_{x_{\min}^p, y_{\min}^p}^{x_{\max}^p, y_{\max}^p} dxdy\ U(x, y, t)$$

where $t_n^{\min}$, $t_n^{\max}$ mark the integration time of the nth exposure; $x_{\min}^p, x_{\max}^p, y_{\min}^p, y_{\max}^p$ mark the region monitored by pixel p; and $U(x, y, t)$ is the photon flux at position x, y and time t. We detail our spatiotemporal frames of reference in the SUPPORTING INFORMATION.

Optics We model $U(x, y, t)$ as consisting of background $U_{\text{back}}(x, y, t)$ and fluorophore photon contributions, *i.e.*, flux, from every imaged light emitter $U^m_{\text{fluor}}(x, y, t)$. These are additive

$$U(x, y, t) = U_{\text{back}}(x, y, t) + \sum_{m=1}^{B} U^m_{\text{fluor}}(x, y, t).$$

Specifically, for the latter, we consider a total of B emitters that we label with $m = 1, \ldots, B$. Each of our emitters is characterized by a position $X^m(t), Y^m(t), Z^m(t)$, all of which may change through time. Since the total number B of imaged emitters is a *critical unknown quantity,* in the next section we describe how we modify the flux $U(x, y, t)$ to allow for a varying number of emitters and in the SUPPORTING INFORMATION we describe how this flux is related to $X^m(t), Y^m(t), Z^m(t)$.

Model inference

The quantities that we are interested in estimating, for example the positions $X^{1:B}(t), Y^{1:B}(t), Z^{1:B}(t)$, are *unknown variables* in the preceding formulation. The total number of such variables depends upon the number of imaged emitters B, which in SRM remains unknown thereby prohibiting processing of the images under the flux $U(x, y, t)$. Since B has such subtle effect, we *modify* our formulation to make it compatible with the nonparametric paradigm of Data Analysis that allows for processing under an unspecified number of variables [53, 36, 49, 12, 35].

In particular, following the nonparametric latent feature paradigm [49, 12], we introduce *indicator* parameters b^m that adopt only values 0 or 1 and recast $U(x, y, t)$ in the form

$$U(x, y, t) = U_{\text{back}}(x, y, t) + \sum_{m=1}^{M} b^m U^m_{\text{fluor}}(x, y, t).$$

Specifically, with the introduction of the indicators, we *increase* the number of emitters represented in our model from B to a number $M > B$ that may be *arbitrarily large.* The critical advantage is that now the total number of model emitters M may be set before processing in contrast with the total number of actual emitters B that remains unknown. With this formulation we infer the values of $b^{1:M}$ during processing, simultaneously with the other parameters of interest. This way, we can actively recruit, *i.e.*, $b^m = 1$, or discard, *i.e.*, $b^m = 0$, light emitters consistently avoiding under/overfitting. Following image processing, our analysis recovers the total number of imaged emitters by the sum $B = \sum_{m=1}^{M} b^m$ and the positions of the emitters $X^m(t), Y^m(t), Z^m(t)$ by the estimated positions of those model emitters with $b^m = 1$. However, a side-effect of introducing M is that our analysis results may depend on the particular value chosen. To *relax* this dependence, we use a *specialized nonparametric prior* on b^m that we describe in detail in the SUPPORTING INFORMATION. This prior specifically allows for image processing at the formal limit $M \to \infty$.

Our overall formulation also includes additional parameters, for example background photon fluxes and fluorophore brightness, that may or may not be of immediate interest. To provide a flexible computational scheme, that works around both unknowns types, *i.e.*, parametric and nonparametric, and also allows for future extensions, we adopt a *Bayesian* approach in which we prescribe prior probability distributions on every unknown parameter beyond just the indicators b^m. These priors, combined with the preceding formulation, lead to the *posterior probability distribution* $p(\theta|w^{1:P}_{1:N})$, where θ gathers every unknown, on which our results rely. We describe the full posterior distribution and its evaluation in the SUPPORTING INFORMATION.

Image acquisition

Experimental timelapse images

Fluorescence timelapse images of U2OS cells injected with chemically labeled firefly luciferase mRNAs were acquired simultaneously on two cameras. Cell culture and handling of U2OS cells prior to injections were performed as previously described [39]. Firefly luciferase mRNAs were *in vitro* transcribed, capped and polyadenylated, and a variable number of Cy3 dyes were non specifically added to the polyA tail using CLICK chemistry [8]. Cells were injected with a solution of Cy3 labeled mRNAs and Cascade Blue labeled 10 kDa dextran (Invitrogen D1976) using a Femtojet pump and Injectman NI2 micromanipulator (Eppendorf) at 20 hPa for 0.1 s with 20 hPa compensation pressure. Successfully injected cells were identified by the presence of a fluorescent dextran and were imaged 30 minutes post injection. Cells were continuously illuminated with the 532 nm laser in HILO mode, and Cy3 fluorescence was collected using a 60x 1.49 NA oil objective. Images were captured simultaneously on two Andor X-10 EMCCD cameras by using a 50:50 beamsplitter, with a 100 ms exposure time.

Synthetic timelapse images

We acquire the validation and benchmarking data through standard computer simulations. We start from *ground truth* as specified in the captions of figs. 4 and 5 and then added noise with values we estimated from the experimental timelapse images according to appendix E.

Acknowledgements

We thank NIH NIGMS (R01GM130745) for supporting early efforts in nonparametrics and tracking, NIH NIGMS (R01GM134426) for supporting single photon efforts, and NIH MIRA entitled "Toward high spatiotemporal resolution models of single molecules for in vivo applications".

References

[1] F. Balzarotti, Y. Eilers, K. C. Gwosch, A. H. Gynnå, V. Westphal, F. D. Stefani, J. Elf, and S. W. Hell. Nanometer resolution imaging and tracking of fluorescent molecules with minimal photon fluxes. *Science*, 355(6325):606–612, 2017.

[2] E. Betzig, G. H. Patterson, R. Sougrat, O. W. Lindwasser, S. Olenych, J. S. Bonifacino, M. W. Davidson, J. Lippincott-Schwartz, and H. F. Hess. Imaging intracellular fluorescent proteins at nanometer resolution. *Science*, 313(5793):1642–1645, 2006.

[3] K. Celler, G. P. van Wezel, and J. Willemse. Single particle tracking of dynamically localizing tata complexes in streptomyces coelicolor. *Biochemical and biophysical research communications*, 438(1):38–42, 2013.

[4] N. Chenouard, I. Bloch, and J.-C. Olivo-Marin. Multiple hypothesis tracking for cluttered biological image sequences. *IEEE transactions on pattern analysis and machine intelligence*, 35(11):2736–3750, 2013.

[5] N. Chenouard, I. Smal, F. De Chaumont, M. Maška, I. F. Sbalzarini, Y. Gong, J. Cardinale, C. Carthel, S. Coraluppi, M. Winter, et al. Objective comparison of particle tracking methods. *Nature methods*, 11(3):281–289, 2014.

[6] I. I. Cisse, I. Izeddin, S. Z. Causse, L. Boudarene, A. Senecal, L. Muresan, C. Dugast-Darzacq, B. Hajj, M. Dahan, and X. Darzacq. Real-time dynamics of rna polymerase ii clustering in live human cells. *Science*, 341(6146):664–667, 2013.

[7] S. Coraluppi and C. Carthel. Multi-stage multiple-hypothesis tracking. *J. Adv. Inf. Fusion*, 6(1):57–67, 2011.

[8] T. C. Custer and N. G. Walter. In vitro labeling strategies for in cellulo fluorescence microscopy of single ribonucleoprotein machines. *Protein Science*, 26(7):1363–1379, 2017.

[9] F. De Chaumont, S. Dallongeville, N. Chenouard, N. Hervé, S. Pop, T. Provoost, V. Meas-Yedid, P. Pankajakshan, T. Lecomte, Y. Le Montagner, et al. Icy: an open bioimage informatics platform for extended reproducible research. *Nature methods*, 9(7):690–696, 2012.

[10] K. N. Fish. Total internal reflection fluorescence (tirf) microscopy. *Current protocols in cytometry*, 50(1):12–18, 2009.

[11] N. Galvanetto, M. T. Ivanović, A. Chowdhury, A. Sottini, M. Nüesch, D. Nettels, R. Best, and B. Schuler. Ultrafast molecular dynamics observed within a dense protein condensate. *bioRxiv*, pages 2022–12, 2022.

[12] Z. Ghahramani. Probabilistic machine learning and artificial intelligence. *Nature*, 521(7553):452–459, 2015.

[13] W. J. Godinez, M. Lampe, R. Eils, B. Müller, and K. Rohr. Tracking multiple particles in fluorescence microscopy images via probabilistic data association. In *2011 IEEE International Symposium on Biomedical Imaging: From Nano to Macro*, pages 1925–1928. IEEE, 2011.

[14] M. G. Gustafsson. Surpassing the lateral resolution limit by a factor of two using structured illumination microscopy. *Journal of microscopy*, 198(2):82–87, 2000.

[15] A. S. Hansen, M. Woringer, J. B. Grimm, L. D. Lavis, R. Tjian, and X. Darzacq. Robust model-based analysis of single-particle tracking experiments with spot-on. *Elife*, 7:e33125, 2018.

[16] K. B. Harpsøe, M. I. Andersen, and P. Kjægaard. Bayesian photon counting with electron-multiplying charge coupled devices (EMCCDs). *Astronomy & Astrophysics*, 537:A50, 2012.

[17] S. W. Hell and J. Wichmann. Breaking the diffraction resolution limit by stimulated emission: stimulated-emission-depletion fluorescence microscopy. *Opt. Lett.*, 19(11):780–782, Jun 1994.

[18] M. Hirsch, R. J. Wareham, M. L. Martin-Fernandez, M. P. Hobson, and D. J. Rolfe. A stochastic model for electron multiplication charge-coupled devices – from theory to practice. *PLOS ONE*, 8(1):1–13, 01 2013.

[19] S. J. Holden, T. Pengo, K. L. Meibom, C. Fernandez Fernandez, J. Collier, and S. Manley. High throughput 3d super-resolution microscopy reveals caulobacter crescentus in vivo z-ring organization. *Proceedings of the National Academy of Sciences*, 111(12):4566–4571, 2014.

[20] M. Husain, T. Boudier, P. Paul-Gilloteaux, I. Casuso, and S. Scheuring. Software for drift compensation, particle tracking and particle analysis of high-speed atomic force microscopy image series. *Journal of Molecular Recognition*, 25(5):292–298, 2012.

[21] A. P. Jalihal, S. Pitchiaya, L. Xiao, P. Bawa, X. Jiang, K. Bedi, A. Parolia, M. Cieslik, M. Ljungman, A. M. Chinnaiyan, et al. Multivalent proteins rapidly and reversibly phase-separate upon osmotic cell volume change. *Molecular cell*, 79(6):978–990, 2020.

[22] A. P. Jalihal, A. Schmidt, G. Gao, S. R. Little, S. Pitchiaya, and N. G. Walter. Hyperosmotic phase separation: Condensates beyond inclusions, granules and organelles. *Journal of Biological Chemistry*, 296, 2021.

[23] K. Jaqaman, D. Loerke, M. Mettlen, H. Kuwata, S. Grinstein, S. L. Schmid, and G. Danuser. Robust single-particle tracking in live-cell time-lapse sequences. *Nature Methods*, 5(8):695–702, Aug. 2008.

[24] S. Jazani, L. W. Xu, I. Sgouralis, D. P. Shepherd, and S. Pressé. Computational proposal for tracking multiple molecules in a multifocus confocal setup. *ACS photonics*, 9(7):2489–2498, 2022.

[25] R. Jungmann, M. S. Avendaño, J. B. Woehrstein, M. Dai, W. M. Shih, and P. Yin. Multiplexed 3d cellular super-resolution imaging with dna-paint and exchange-paint. *Nature methods*, 11(3):313–318, 2014.

[26] J. D. Karslake, E. D. Donarski, S. A. Shelby, L. M. Demey, V. J. DiRita, S. L. Veatch, and J. S. Biteen. Smaug: Analyzing single-molecule tracks with nonparametric bayesian statistics. *Methods*, 193:16–26, 2021.

[27] I. M. Khater, I. R. Nabi, and G. Hamarneh. A review of super-resolution single-molecule localization microscopy cluster analysis and quantification methods. *Patterns*, 1(3):100038, 2020.

[28] Z. Kilic, I. Sgouralis, W. Heo, K. Ishii, T. Tahara, and S. Pressé. Extraction of rapid kinetics from smfret measurements using integrative detectors. *Cell Reports Physical Science*, 2(5):100409, 2021.

[29] J. Kim, J. Y. Kim, S. Jeon, J. W. Baik, S. H. Cho, and C. Kim. Super-resolution localization photoacoustic microscopy using intrinsic red blood cells as contrast absorbers. *Light: Science & Applications*, 8(1):103, 2019.

[30] T. A. Klar, S. Jakobs, M. Dyba, A. Egner, and S. W. Hell. Fluorescence microscopy with diffraction resolution barrier broken by stimulated emission. *Proc. Natl. Acad. Sci. U.S.A.*, 97(15):8206–8210, 2000.

[31] P. Kowalek, H. Loch-Olszewska, and J. Szwabiński. Classification of diffusion modes in single-particle tracking data: Feature-based versus deep-learning approach. *Physical Review E*, 100(3):032410, 2019.

[32] A. Lee, K. Tsekouras, C. Calderon, C. Bustamante, and S. Pressé. Unraveling the thousand word picture: An introduction to super-resolution data analysis. *Chemical Reviews*, 117(11):7276–7330, 2017.

[33] L. Liang, H. Shen, P. De Camilli, and J. S. Duncan. Tracking clathrin coated pits with a multiple hypothesis based method. In *Medical Image Computing and Computer-Assisted Intervention–MICCAI 2010: 13th International Conference, Beijing, China, September 20-24, 2010, Proceedings, Part II 13*, pages 315–322. Springer, 2010.

[34] E. Meijering, O. Dzyubachyk, and I. Smal. Methods for cell and particle tracking. *Methods in enzymology*, 504:183–200, 2012.

[35] P. Müller, F. A. Quintana, A. Jara, and T. Hanson. *Bayesian nonparametric data analysis*, volume 1. Springer, 2015.

[36] P. Orbanz and Y. W. Teh. Bayesian nonparametric models. *Encyclopedia of machine learning*, 1, 2010.

[37] J. Otterstrom, A. Castells-Garcia, C. Vicario, P. A. Gomez-Garcia, M. P. Cosma, and M. Lakadamyali. Super-resolution microscopy reveals how histone tail acetylation affects dna compaction within nucleosomes in vivo. *Nucleic acids research*, 47(16):8470–8484, 2019.

[38] E. P. Perillo, Y.-L. Liu, K. Huynh, C. Liu, C.-K. Chou, M.-C. Hung, H.-C. Yeh, and A. K. Dunn. Deep and high-resolution three-dimensional tracking of single particles using nonlinear and multiplexed illumination. *Nature Communications*, 6(1):7874, 2015.

[39] S. Pitchiaya, V. Krishnan, T. C. Custer, and N. G. Walter. Dissecting non-coding rna mechanisms in cellulo by single-molecule high-resolution localization and counting. *Methods*, 63(2):188–199, 2013.

[40] S. Pitchiaya, M. D. Mourao, A. P. Jalihal, L. Xiao, X. Jiang, A. M. Chinnaiyan, S. Schnell, and N. G. Walter. Dynamic recruitment of single rnas to processing bodies depends on rna functionality. *Molecular cell*, 74(3):521–533, 2019.

[41] S. Ram, P. Prabhat, J. Chao, E. Sally Ward, and R. J. Ober. High accuracy 3d quantum dot tracking with multifocal plane microscopy for the study of fast intracellular dynamics in live cells. *Biophysical Journal*, 95(12):6025–6043, 2008.

[42] L. Rayleigh. XXXI. investigations in optics, with special reference to the spectroscope. *The London, Edinburgh, and Dublin Philosophical Magazine and Journal of Science*, 8(49):261–274, 1879.

[43] E. G. Reynaud, J. Peychl, J. Huisken, and P. Tomancak. Guide to light-sheet microscopy for adventurous biologists. *Nature methods*, 12(1):30–34, 2015.

[44] M. J. Rust, M. Bates, and X. Zhuang. Sub-diffraction-limit imaging by stochastic optical reconstruction microscopy (STORM). *Nature methods*, 3(10):793–796, 2006.

[45] J. Schnitzbauer, M. T. Strauss, T. Schlichthaerle, F. Schueder, and R. Jungmann. Super-resolution microscopy with DNA-PAINT. *Nature protocols*, 12(6):1198–1228, 2017.

[46] M. Shayegan, R. Tahvildari, K. Metera, L. Kisley, S. W. Michnick, and S. R. Leslie. Probing inhomogeneous diffusion in the microenvironments of phase-separated polymers under confinement. *Journal of the American Chemical Society*, 141(19):7751–7757, 2019.

[47] J.-Y. Tinevez, N. Perry, J. Schindelin, G. M. Hoopes, G. D. Reynolds, E. Laplantine, S. Y. Bednarek, S. L. Shorte, and K. W. Eliceiri. Trackmate: An open and extensible platform for single-particle tracking. *Methods*, 115:80–90, 2017. Image Processing for Biologists.

[48] M. Tokunaga, N. Imamoto, and K. Sakata-Sogawa. Highly inclined thin illumination enables clear single-molecule imaging in cells. *Nature methods*, 5(2):159–161, 2008.

[49] R. van de Schoot, S. Depaoli, R. King, B. Kramer, K. Märtens, M. G. Tadesse, M. Vannucci, A. Gelman, D. Veen, J. Willemsen, et al. Bayesian statistics and modelling. *Nature Reviews Methods Primers*, 1(1):1–26, 2021.

[50] F. J. Verweij, L. Balaj, C. M. Boulanger, D. R. Carter, E. B. Compeer, G. D'angelo, S. El Andaloussi, J. G. Goetz, J. C. Gross, V. Hyenne, et al. The power of imaging to understand extracellular vesicle biology in vivo. *Nature methods*, 18(9):1013–1026, 2021.

[51] L. von Diezmann, Y. Shechtman, and W. Moerner. Three-dimensional localization of single molecules for super-resolution imaging and single-particle tracking. *Chemical reviews*, 117(11):7244–7275, 2017.

[52] U. von Toussaint. Bayesian inference in physics. *Rev. Mod. Phys.*, 83:943–999, Sep 2011.

[53] L. Wasserman. *All of nonparametric statistics*. Springer Science & Business Media, 2006.

[54] N. P. Wells, G. A. Lessard, P. M. Goodwin, M. E. Phipps, P. J. Cutler, D. S. Lidke, B. S. Wilson, and J. H. Werner. Time-resolved three-dimensional molecular tracking in live cells. *Nano letters*, 10(11):4732–4737, 2010.

[55] N. P. Wells, G. A. Lessard, and J. H. Werner. Confocal, three-dimensional tracking of individual quantum dots in high-background environments. *Analytical chemistry*, 80(24):9830–9834, 2008.

[56] K. I. Willig, S. O. Rizzoli, V. Westphal, R. Jahn, and S. W. Hell. Sted microscopy reveals that synaptotagmin remains clustered after synaptic vesicle exocytosis. *Nature*, 440(7086):935–939, 2006.

[57] M. R. Winter, C. Fang, G. Banker, B. Roysam, and A. R. Cohen. Axonal transport analysis using multi-temporal association tracking. *International journal of computational biology and drug design*, 5(1):35–48, 2012.

[58] L. Yang, Z. Qiu, A. H. Greenaway, and W. Lu. A new framework for particle detection in low-snr fluorescence live-cell images and its application for improved particle tracking. *IEEE transactions on biomedical engineering*, 59(7):2040–2050, 2012.

[59] Z. Yin, T. Kanade, and M. Chen. Understanding the phase contrast optics to restore artifact-free microscopy images for segmentation. *Medical image analysis*, 16(5):1047–1062, 2012.